ARTICLES
https://doi.org/10.1038/s41561-020-0593-2
nature geoscience

Global distribution of sediment-hosted metals controlled by craton edge stability

Mark J. Hoggard[1,2]✉, Karol Czarnota[3,4]✉, Fred D. Richards[1,5], David L. Huston[3], A. Lynton Jaques[4] and Sia Ghelichkhan[4]

Sustainable development and the transition to a clean-energy economy drives ever-increasing demand for base metals, substantially outstripping the discovery rate of new deposits and necessitating dramatic improvements in exploration success. Rifting of the continents has formed widespread sedimentary basins, some of which contain large quantities of copper, lead and zinc. Despite over a century of research, the geological structure responsible for the spatial distribution of such fertile regions remains enigmatic. Here, we use statistical tests to compare deposit locations with new maps of lithospheric thickness, which outline the base of tectonic plates. We find that 85% of sediment-hosted base metals, including all giant deposits (>10 megatonnes of metal), occur within 200 kilometres of the transition between thick and thin lithosphere. Rifting in this setting produces greater subsidence and lower basal heat flow, enlarging the depth extent of hydrothermal circulation available for forming giant deposits. Given that mineralization ages span the past two billion years, this observation implies long-term lithospheric edge stability and a genetic link between deep Earth processes and near-surface hydrothermal mineral systems. This discovery provides an unprecedented global framework for identifying fertile regions for targeted mineral exploration, reducing the search space for new deposits by two-thirds on this lithospheric thickness criterion alone.

Consumption of base metals (copper, lead, zinc and nickel) over the next ~25 years is set to exceed the total produced in human history to date[1,2]. Moreover, critical minerals (for example, cobalt, indium and germanium) are often produced as by-products of base metal mining and are essential in many high-tech applications[3–7]. A growing concern is that the rate of exploitation of existing reserves is outstripping discovery of new deposits, despite exploration expenditure tripling during the 2005–2012 minerals boom[1,2]. To reverse this trend and supply the resources necessary to comply with policies such as the Paris Climate Agreement and United Nations' Sustainable Development Goals, improved techniques for locating new deposits are required, particularly those buried under shallow sedimentary cover or ice[8].

Narrowing the search space for new deposits

In mineral exploration, initial area selection at continental scales is arguably the most important step, as successful identification of fertile regions can compensate for many subsequent errors[9]. Over the past two decades, the search for analogues of known deposits has progressed towards a more holistic determination of factors controlling deposit generation and preservation[10–14]. Mineral systems analysis has resulted in a growing acceptance that the spatial distribution of deposits associated with magmatic processes is controlled by lithospheric-scale structure[9,15,16]. For example, porphyry copper deposits are generated by wet melting in the mantle wedge above a subducting slab, followed by emplacement of these melts into the shallow overlying crust and subsequent concentration by high-temperature hydrothermal circulation[16]. Thus, by combining the plate tectonic setting with geological constraints on the location of key mineral system ingredients, the search space for new magmatic deposits can be substantially reduced [17–19].

In the case of sediment-hosted deposits, most assessments to date have focused on their genesis within the context of Earth's secular evolution, as well as past tectonic and geographic settings[20]. The majority are found in failed rift and passive margin settings, and it is generally agreed that basin-scale hydrothermal circulation is required to scavenge sufficient metals to form giant deposits (Fig. 1a)[21–23]. Metals are mobilized and transported by oxidized brines with moderate temperatures (80–250 °C) and moderate-to-high salinity (10–30 wt.% NaCl), limiting their maximum age to the Great Oxidation Event at 2.4 billion years ago (Ga)[21,22]. These fluids are sourced from evaporites at low latitudes and remain buffered as they pass through voluminous oxidized terrestrial sediments, allowing them to scavenge lead from arkosic sandstones and felsic volcanics, as well as copper and zinc from mafic rocks[21,22]. Transport along faults, during either rifting or basin inversion, focuses these fluids into oxidation–reduction interfaces, such as distal-facies black shales, where metals precipitate (Fig. 1b,c) [24].

Sediment-hosted base metal deposits are desirable due to their greater quantity of contained metal (in contrast to volcanogenic massive sulfides) and higher grades of ore (compared with porphyry copper), resulting in lower environmental degradation during extraction[6,25]. However, narrowing the search space for new sediment-hosted deposits has been less successful than for magmatic mineral systems. Sedimentary basins cover ~75% of the continental surface, and the key ingredients of evaporites associated with brine formation, felsic and mafic volcanic rocks for sourcing metals, and organic-rich-shale precipitation sites are widespread and do not substantially reduce this search space. The first-order geological control that localizes their spatial distribution throughout the continents remains unknown, severely limiting predictive power for identifying new targets. A classic example comes from the

[1]Department of Earth and Planetary Sciences, Harvard University, Cambridge, MA, USA. [2]Lamont-Doherty Earth Observatory, Columbia University, New York, NY, USA. [3]Geoscience Australia, Canberra, Australian Capital Territory, Australia. [4]Research School of Earth Sciences, Australian National University, Canberra, Australian Capital Territory, Australia. [5]Department of Earth Science and Engineering, Imperial College, London, UK.
✉e-mail: mark_hoggard@fas.harvard.edu; karol.czarnota@ga.gov.au

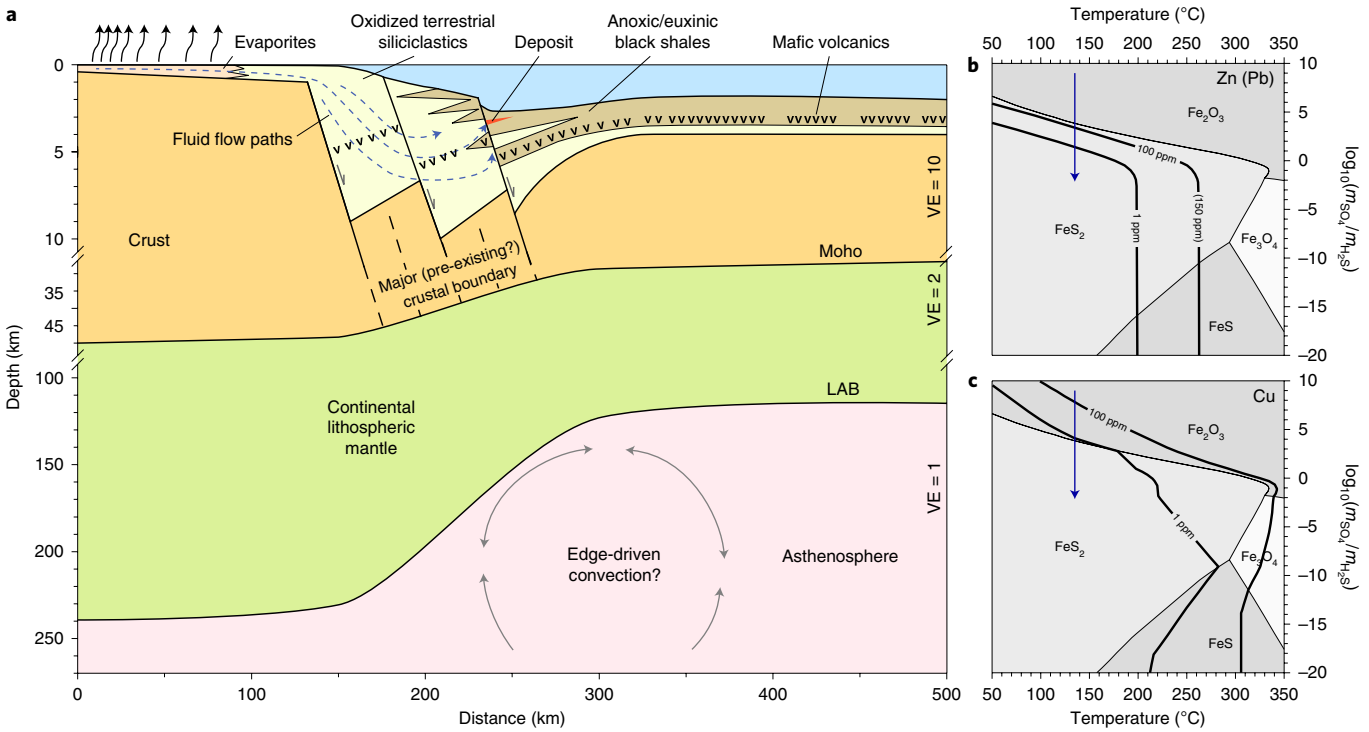

Fig. 1 | Mineralization system for genesis of sediment-hosted base metal deposits. a, Schematic illustration of deposit location in extensional rift settings. Basinal brines sourced from evaporites scavenge metals from oxidized terrestrial sediments and volcanics (v) on route to metal deposition sites in black shales[23]. Notice variable vertical exaggeration (VE) and prominence of the lithosphere–asthenosphere boundary (LAB) edge illustrated at 1/1 scale. Schematic based on architectural constraints from the Australian Carpentaria Zinc Belt and Polish Fore-Sudetic Block. **b**, Stability field of Fe–S–O minerals as a function of temperature and redox conditions; m_{SO_4}, molarity of sulfate; m_{H_2S}, molarity of sulfide; thick black lines, solubility of zinc (and lead) in brine[24], calculated for fluid salinity = 10 wt.% NaCl, total concentration of sulfur species = $10^{-2.5}$ M and pH = 4.5; blue arrow, fluid path for metal precipitation by oxidation–reduction deposition mechanism. **c**, Same as **b** for copper solubility.

Carpentaria Zinc Belt in northern Australia, which contains several world-class clastic-dominated lead–zinc (PbZn-CD) deposits formed between 1.8 and 1.4 Ga (Fig. 2a). These deposits lie along an arcuate trend that runs oblique to mapped geology and crustal geological boundaries, as demonstrated by gravity and magnetic datasets [26].

Crucially, despite the absence of a clear crustal relationship, the linear distribution of sediment-hosted deposits in the Carpentaria Zinc Belt hints at an underlying regional-scale control. An important advance in understanding the genesis of magmatic mineral systems has come from probing their relationship with major crustal and lithospheric structures[16]. Given that sedimentary basins are themselves the result of lithospheric-scale processes, we investigate both regional- and global-scale links between sediment-hosted base metal deposits and the most fundamental shallow mantle structure, the lithosphere–asthenosphere boundary (LAB).

Relationship with lithospheric structure

We begin by collating global inventories of six major base metal mineral systems from published sources (Methods). Three are magmatic and three are sediment-hosted, which include sedimentary copper (Cu-sed), PbZn-CD (commonly also referred to as sedimentary exhalative), and Mississippi Valley-type lead–zinc (PbZn-MVT). We next refine a method developed by Priestley and McKenzie[27] for mapping the thermal LAB from seismic tomography, taking into consideration recent laboratory experiments[28] concerning the effect of anelasticity on shear-wave velocities (Methods). This benchmarking procedure is necessary to increase consistency between LAB maps obtained for different tomography models, which can image surprisingly variable seismic velocities. A high-resolution regional LAB map over Australia is obtained from the **FR12** model[29] and is calibrated using nine local palaeogeotherms derived from thermobarometry of mantle peridotite xenoliths and xenocrysts. To expand our analysis to other continents, a global LAB is also produced using the **SL2013sv** model[30] and calibrated using multiple constraints, including the latest thermal structure of cooling oceanic lithosphere[31]. This global LAB exhibits a bimodal thickness distribution, with peaks at 90 km and 190 km, separated by a minimum at 150 km (Supplementary Information).

Inspection of the Australian model reveals a striking correlation between major sediment-hosted mineral deposits and the edge of thick lithosphere, defined here by the 170-km thickness contour (Fig. 2b). Major PbZn-CD and sedimentary copper deposits in the Carpentaria Zinc Belt overlie this contour, which runs obliquely to geological boundaries such that intersections between these two features consistently coincide with deposit locations. This behaviour is particularly useful for highlighting new prospective regions for exploration. Other observables that correlate with this lithospheric thickness change include variations in lead isotopes from Proterozoic galena and pyrite minerals[32], long-wavelength gravity anomaly gradients[33], changes in crustal character in deep-reflection seismic profiles[34], a topographic ridge and the western extent of Cretaceous marine sediments (Fig. 2a). These latter two associations demonstrate the post-Proterozoic stability of this edge and its influence on local geology and topography. There is also a strong relationship with iron oxide–copper–gold (IOCG) deposits, including the Olympic Dam mine in South Australia (84 Mt of copper, the world's largest known uranium resource)[35–37]. However, a lack

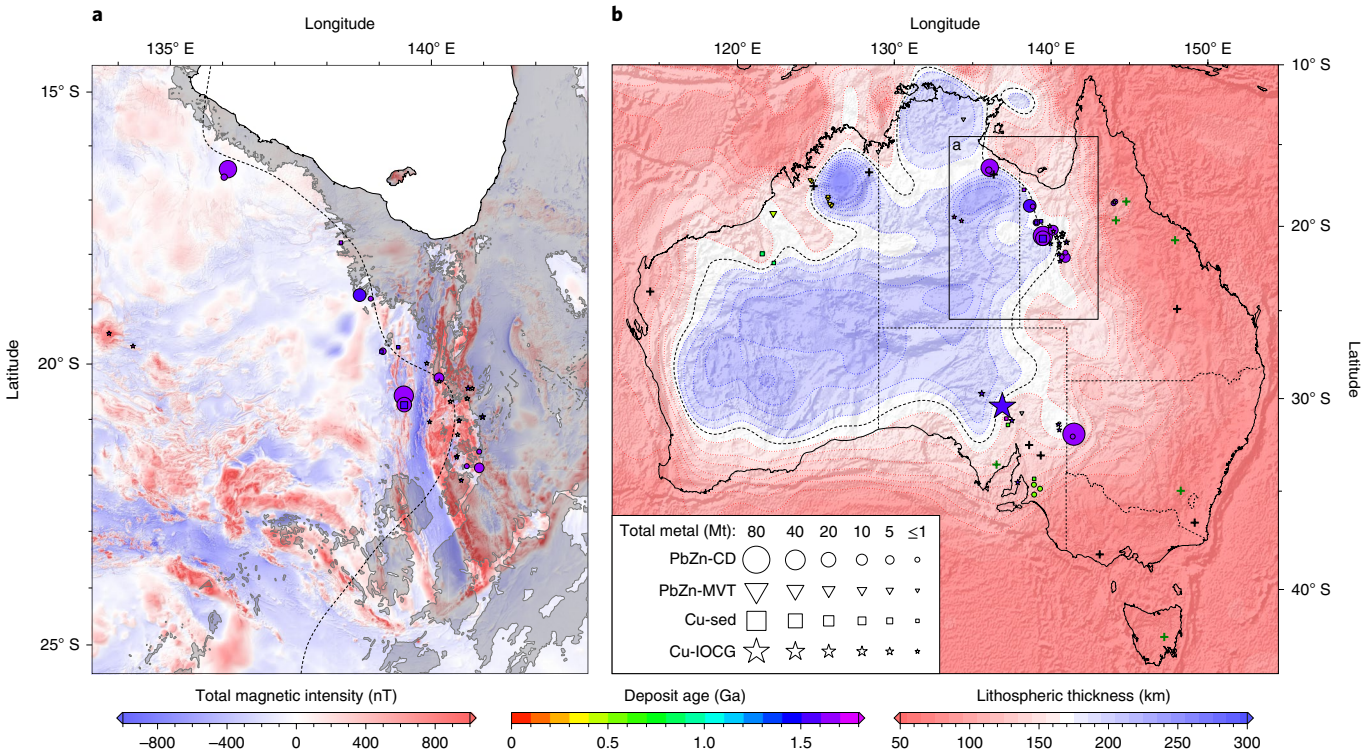

Fig. 2 | Distribution of sediment-hosted and IOCG base metal deposits as a function of Australian lithospheric thickness. a, Carpentaria Zinc Belt; red/blue, variably reduced to pole aeromagnetic intensity data[26]; grey polygons, generalized outcrop of Cretaceous marine sediments in Eromanga and Carpentaria Basins[51]; black dashed contour, 170-km LAB thickness; symbols, deposit locations; symbol area proportional to estimate of total contained mass of metal (either lead plus zinc, or copper) in megatonnes (Mt); unknown deposit size given 1 Mt symbol; colour, ore body formation age (Ga); unknown age plotted in grey. **b**, Australian LAB mapped by converting **FR12** tomography[29] to temperature using an anelasticity parameterization[28] calibrated on local palaeogeotherms (Methods) and illuminated by free-air gravity anomalies[26]; black/green crosses, location of geotherms used as constraints/tests in anelasticity calibration (Supplementary Information); box, location of panel **a**. Large star in South Australia shows location of the Olympic Dam deposit.

of consensus on global classification schemes means that we have limited analysis of this deposit type to only Australia.

Extending our analysis globally further confirms the strength of this relationship (Fig. 3). The link between the 170-km lithospheric thickness contour and location of all large sediment-hosted deposits holds regardless of deposit age, which spans the past two billion years. Given the 180- to 220-km cluster of LAB thicknesses is likely to represent standard cratonic lithosphere, the 170-km contour therefore demarcates the outer boundary of cratons. Within the PbZn-CD deposit class, those more strongly associated with abundant mafic rocks systematically occur on the thinner lithosphere side of the contour compared with their carbonate-rich counterparts (for example, Carpentaria Zinc Belt and northwest North America). These observations are consistent with an extensional origin of the host basins.

To quantify these visual relationships, the shortest distance is calculated between each deposit and the 170-km LAB thickness contour, and results are plotted in a cumulative distribution function (CDF). Weighting deposits by the mass of contained metal and substituting the Australian LAB from the global model with our high-resolution regional version substantially improves the correlation for PbZn-CD (Fig. 4a). Globally, we observe that ~95% of Cu-sed, ~90% of PbZn-CD and ~70% of PbZn-MVT resources are located within a 200-km-wide corridor either side of the 170-km LAB thickness contour (Fig. 4b). This region corresponds to only ~35% of continental surface area. Given that this swath width is similar to the ~280-km node spacing in **SL2013sv**, tighter constraints are only possible with higher-resolution tomography models. For example, all giant deposits in Australia lie within 100 km of the 170-km contour for the higher-resolution **FR12** model. The significance of the relationship is globally examined using the two-sample Kolmogorov–Smirnov test[38], which estimates that the probability of these sediment-hosted deposits representing random continental locations is less than 1 in 10^{12} (Methods). This relationship holds true for three other global surface-wave tomography models (Extended Data Fig. 1).

All >10 Mt sediment-hosted deposits are located along the boundary of thick lithosphere, but among the smaller deposits, there are some notable exceptions. Minor PbZn-CD outliers occur in Europe, the Caribbean, Indonesia and east China. Anomalous PbZn-MVT deposits are found in Ireland, east China and along the Tethys subduction zone across Europe, while small Cu-sed deposits occur in southwestern North America and southern South America. This observation indicates that minor sediment-hosted mineral systems can develop in a variety of basins, while giant deposits form only at the edges of cratonic lithosphere. PbZn-MVT deposits are generally more widely distributed, which likely reflects that a subset of these deposits is linked with orogenic processes along basin margins[21], resulting in longer hydrothermal fluid flow paths. Nevertheless, not all sediment-hosted outliers were necessarily anomalies at the time of ore formation. The majority now occur in accretionary terranes, whereby plate tectonic processes may have rifted segments off thick lithosphere and transported them into subduction zone settings. Other areas, such as east China, are known to have undergone lithospheric thinning some time after deposit formation, based on thermobarometric constraints[39].

Regardless of age, sediment-hosted base metal deposits predominantly cluster on the edges of present-day thick lithosphere.

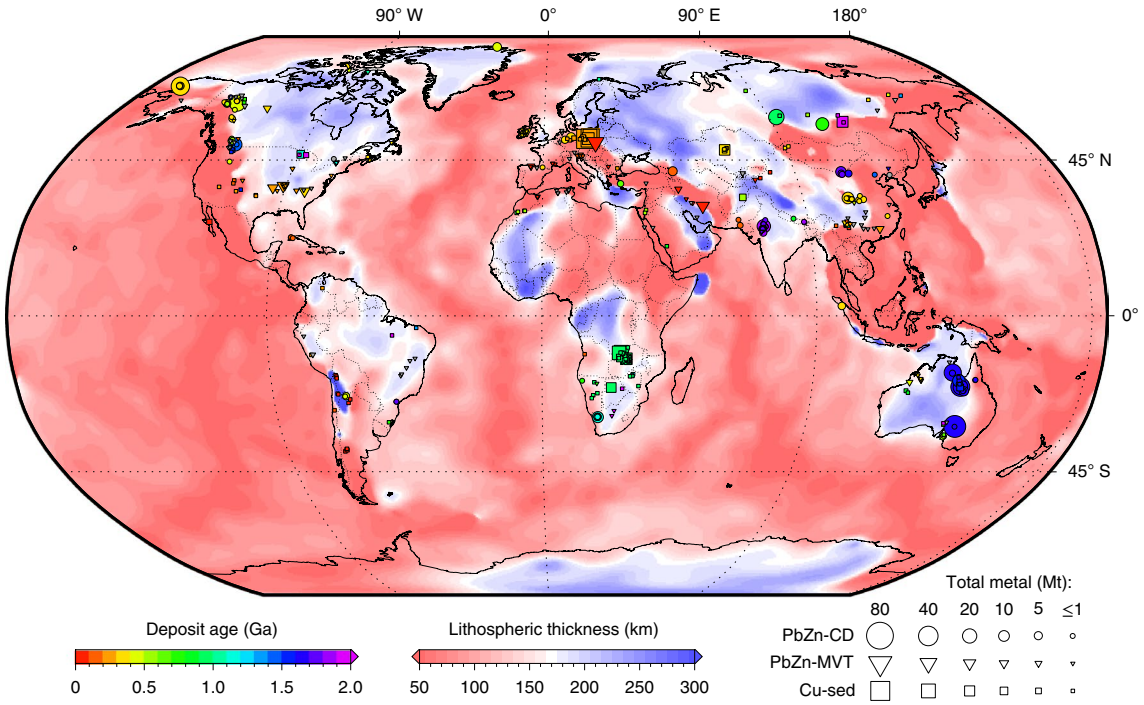

Fig. 3 | Global distribution of sediment-hosted base metal deposits as a function of lithospheric thickness. LAB derived from **SL2013sv** tomography model[30] using a calibrated anelasticity parameterization[28] (Methods). Symbols, deposit locations; symbol area proportional to estimate of total contained mass of metal (either lead plus zinc, or copper) in megatonnes (Mt); unknown deposit size given 1 Mt symbol; colour, ore body formation age (Ga); unknown age plotted in grey.

Therefore, many of these lithospheric steps appear to be remarkably robust on billion-year timescales, despite the assembly and disaggregation of several supercontinents, the impacts of large igneous provinces, and the possible erosional effect of edge-driven convection[40]. Deposit ages in northwestern North America span ~1.5–0.5 Ga, pointing to the stability and importance of this boundary in localizing multiple deformational and ore-forming processes.

Mineral system implications

Our results indicate that the edges of thick lithosphere place first-order controls on the genesis of extensional basins and their associated mineral systems (Fig. 1). Rifting causes localized thinning and produces a lateral transition from oxidizing terrestrial environments into marine settings. This transition provides the optimal juxtaposition of the ingredients necessary for deposit formation. The adjacent unstretched cratons provide a bountiful source of oxidized sediments and extensive low-elevation platforms, which enhance evaporite formation. Proximal land masses also aid the development of restricted marine settings that are ideal for accumulating thick evaporite sequences (through periodic cycles of evaporation and flooding) and promote euxinic water conditions that are favourable for deposition of reducing shales that are high in organic carbon. Thinning of the lithosphere in the centre of the basin causes decompression melting, providing mafic and felsic volcanic rocks from which metals are scavenged. Intercalation of proximal and distal facies components is further modulated by transient vertical motions, generally thought to be associated with edge-driven convection across lithospheric steps[41]. Nevertheless, these mineral system components are common to both rifts in thick lithosphere and regular passive margins, and the question remains — what is favourable about rifting cratonic lithosphere for formation of the shallow hydrothermal systems necessary to produce giant deposits?

From a geodynamic perspective, these lithospheric edges represent rheological contrasts that focus strain and localize repeated cycles of extensional deformation and basin contraction, thereby controlling both the spatial distribution of required lithologies and the focusing of mineralizing fluids[19,42,43]. Thick cratonic lithosphere is colder than standard continental lithosphere and has a larger seismogenic thickness, resulting in the development of deeper, longer, and more widely spaced normal faults during rifting[44]. This architecture increases the horizontal aspect ratio of hydrothermal cells, providing greater sediment volumes for fluid–rock interaction. These faults are active for longer time periods, and the entire syn-rift phase of basin formation can last 50–100 Myr, in contrast to standard continental rifts that typically last ~25 Myr, yielding a more-extensive time window for mineralization[45]. Furthermore, basins forming in continental interiors are more likely to be restricted, which is not only favourable for high siliciclastic supply and the formation of evaporites and reductants, but also results in laterally continuous sediment packages that trap hydrothermal fluid systems and potentially promote recirculation of brines [22].

A key observation is that metal precipitation in sediment-hosted base metal deposits is generally driven by oxidation–reduction reactions, which become ineffective when brine temperatures exceed ~250 °C (Fig. 1b,c)[24]. As hydrothermal fluid temperatures are buffered by conditions towards the base of the sediment pile (often where the mafic metal source rocks are located), the basal temperature of the sedimentary pile must not substantially exceed this threshold value. Total extension in a basin can be estimated using a stretching factor, β, which is the ratio of original to final crustal thickness. Failed rifts on standard continental lithosphere, such as the North Sea, typically have $\beta \approx 2$, and simple thermal modelling assuming pure-shear rifting indicates that this produces ~4 km of syn-rift sediment with basal temperatures cooler than ~250 °C (Fig. 5a and Methods). Given that all the necessary ingredients occur within basins, the likelihood of developing a successful mineral system is higher for a larger sediment pile, which can be achieved by increasing the stretching factor. However, more-extreme rifting causes the asthenosphere to upwell to substantially shallower depths, producing

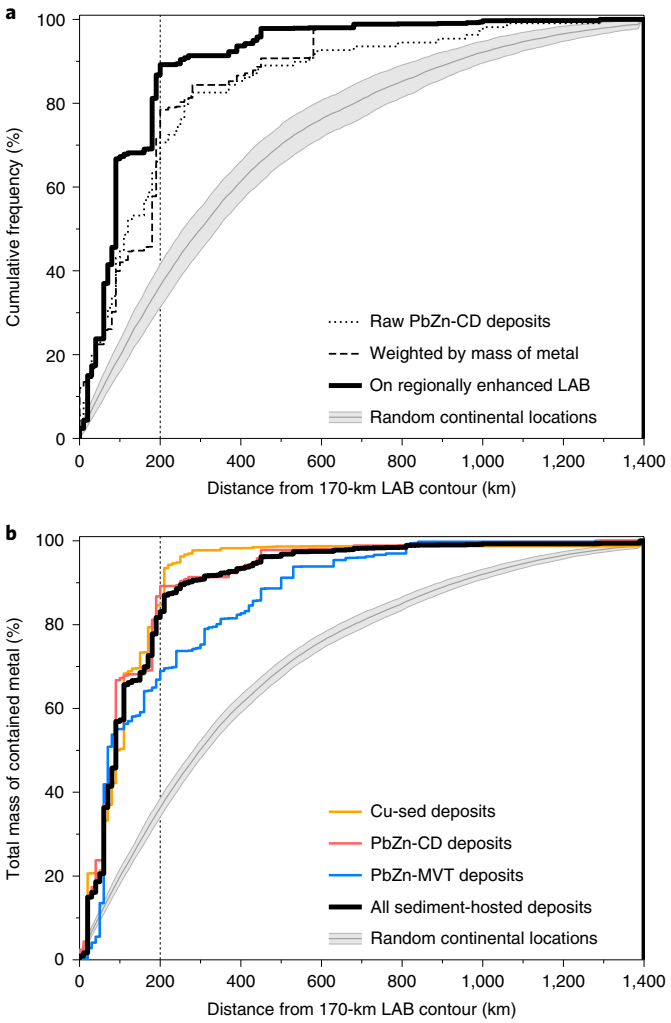

Fig. 4 | CDFs for global sediment-hosted base metals. a, Different approaches for counting 109 PbZn-CD deposits. Dotted line, simple count of number of deposits with increasing distance from the 170-km contour in global LAB map (Fig. 3); dashed line, weighting by contained mass of lead and zinc; solid black line, mass-weighted deposits where the Australian LAB from the global model has been replaced with the regionally enhanced map (Fig. 2b); grey line/bounds, mean and s.d. of 100 sets of equivalent number (109) of randomly drawn continental locations, with respect to regionally enhanced LAB. **b**, Mass-weighted, regionally enhanced CDFs for 139 Cu-sed deposits, 109 PbZn-CD deposits, 147 PbZn-MVT deposits and the combination of all three. Grey band as before for combined number of deposits (395).

elevated basal heat flow that heats the sediment pile above this threshold and so inhibits metal precipitation (Fig. 5b).

Two important differences occur during rifting of cratonic lithosphere. First, the greater initial thickness of the lithosphere results in a lower geothermal gradient, such that the basal heat-flow spike during rifting is substantially lower than for standard continental rifts (Supplementary Information). Second, the density of cratonic lithosphere is reduced by up to ~50 kg m^{-3} by chemical depletion compared with standard lithosphere[46]. This increased buoyancy reduces the dampening effect during syn-rift subsidence that is associated with replacing cold continental lithosphere with lower-density asthenosphere, resulting in substantially larger thicknesses of syn-rift sediments for any given stretching factor. Assuming unlimited sediment supply, $\beta \approx 2$ yields an 8- to 9-km syn-rift sediment pile, the base of which stays cooler than the threshold ~250 °C (Fig. 5c). Thus, rifting cratonic lithosphere produces more than twice the volume of mineral system ingredients without exceeding the thermal conditions necessary for successful precipitation, over a duration that can be up to a factor of four more extensive (Fig. 5d,e). This mechanism explains why smaller deposits can occur in any extensional setting (for example, Irish PbZn-MVT deposits), but giant deposits requiring the largest volumes of fluid–rock interaction are restricted to rift basins at the edges of the thickest lithosphere.

A final consideration is that a setting on the edge of thick lithosphere enhances the preservation potential of deposits through subsequent orogenic events and supercontinent cycles. For example, the Boleo Copper District in Baja California formed only three-million years ago and sits in shallow crust on thin lithosphere, resulting in poor long-term preservation potential. By contrast, the 1.7 Ga Broken Hill deposit in Australia (the world's largest known lead deposit) has been metamorphosed to amphibolite–granulite facies, yet survives on the edge of the Curnamona part of the South Australian craton.

Surprisingly, given the results of previous studies[16], deposits associated with magmatic systems generally exhibit a weaker association with the edge of cratonic lithosphere than sediment-hosted systems (Supplementary Information). Porphyry copper deposits are predominantly Cenozoic in age and are generally positioned on thin lithosphere (≤100 km). Their formation in subduction zone settings at shallow crustal depths leads to poor preservation potential within the geological record, making this association unsurprising. Volcanogenic massive sulfides have an episodic age distribution from 3.5 Ga to present. Their generation is thought to require moderate-degree partial melting of hydrated mantle in back-arc settings[47]. We observe that they spatially occur randomly on thick and thin lithosphere but exhibit systematic temporal ordering, with the oldest positioned over thick lithosphere that are rimmed by progressively younger deposits, consistent with growth of cratons by accretion. Finally, magmatic nickel deposits are mostly Archaean and Proterozoic in age and commonly occur on thick lithosphere (≥150 km). Unlike other base metal deposits, their distribution is associated with edges of even thicker lithosphere (~200 km), broadly consistent with previous studies showing major lithospheric structural controls on these deposit locations[15,48,49]. Their generation requires large-fraction partial melting of peridotite, indicative of high mantle temperatures (more prevalent in an early, hotter Earth) and decompression melting at shallow depths[50]. Therefore, their present distribution suggests lithospheric thickness must have locally increased since formation, simultaneously enhancing preservation potential.

In summary, this work illustrates a new and robust link between giant sediment-hosted base metal mineral systems and the edges of thick lithosphere. Approximately 55% of the world's lead, 45% of its zinc and 20% of known copper are found within ~200 km of this boundary. We have demonstrated the value of regional seismic arrays to better resolve this edge and enhance the mineral exploration efforts required to sustain ongoing global development. Importantly, deposit ages indicate that, following rifting, the edges of thick lithosphere are generally stable over billion-year timescales. The far-reaching geodynamic and societal implications of these observations highlight the need for extensive further research. To improve resolution of mapped lithospheric structure, higher fidelity seismic imaging needs to be coupled with enhanced mantle xenolith coverage and tighter constraints on seismic anelasticity from mineral physics experiments. More generally, these maps should be integrated with models of basin dynamics, surface processes and reactive transport modelling, and they should be benchmarked against additional geological information, such as sedimentary facies variations, tectonic structures and alteration zones. These multiple research strands will yield fundamental new insights into sediment-hosted mineral systems and lead to substantial improvements in exploration success.

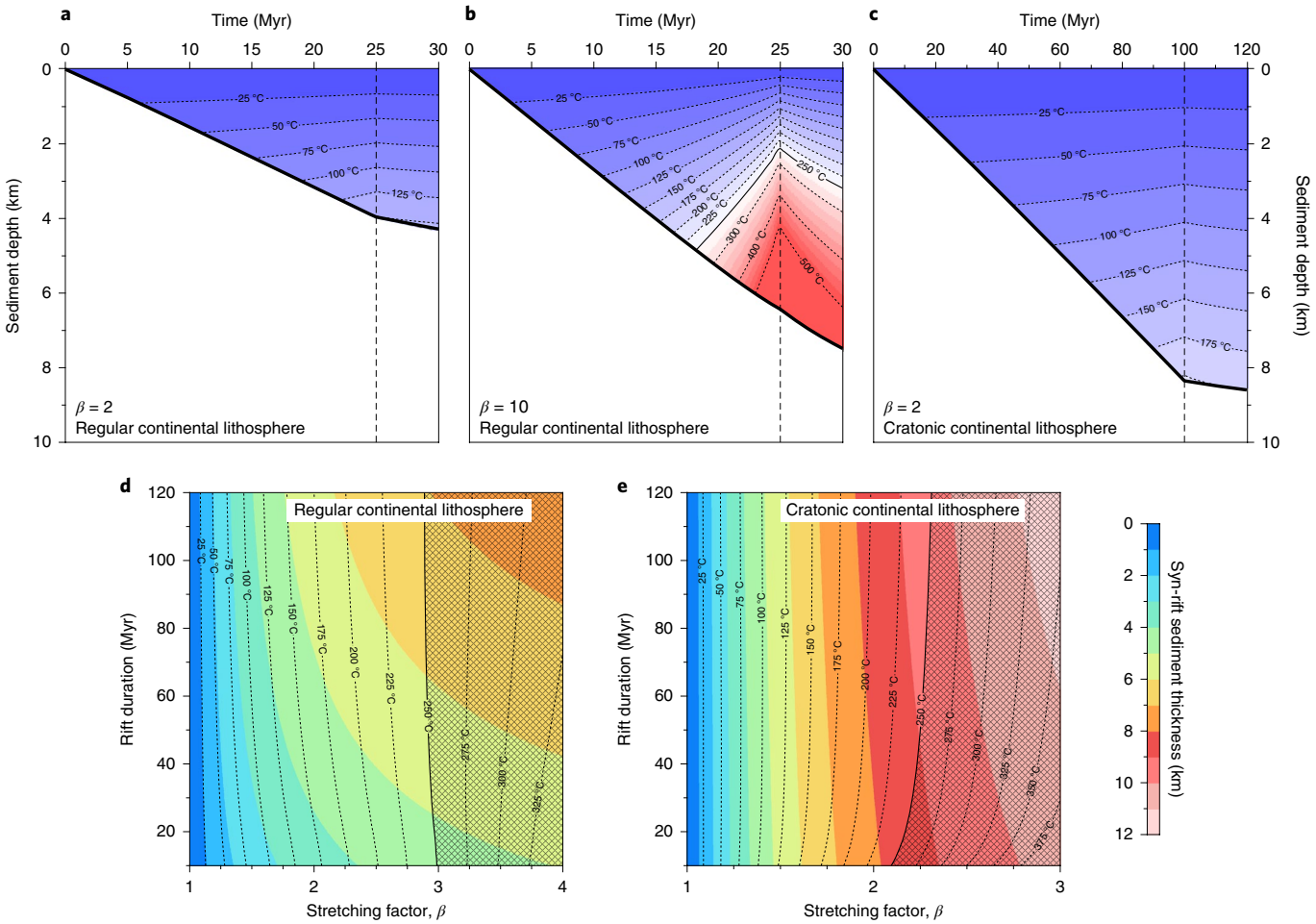

Fig. 5 | Thermal modelling of basin subsidence histories. a, Syn-rift sedimentation for $\beta = 2$ rift of regular continental lithosphere; dashed line, rift duration; colours, temperature structure of the sediment pile. **b**, Same as **a** for $\beta = 10$ rift of regular continental lithosphere. **c**, Same as **a** for $\beta = 2$ rift of cratonic continental lithosphere. **d**, Minerals system operating window for rifting of regular continental lithosphere; colours, syn-rift sediment thickness; contours, basal temperature of the sediment pile; hatched region, location where hydrothermal fluids typically become too hot for metal precipitation by oxidation–reduction mechanisms (>250 °C). **e**, Same as **d** for cratonic continental lithosphere.

Online content

Any methods, additional references, Nature Research reporting summaries, source data, extended data, supplementary information, acknowledgements, peer review information; details of author contributions and competing interests; and statements of data and code availability are available at https://doi.org/10.1038/s41561-020-0593-2.

Received: 2 April 2019; Accepted: 15 May 2020;
Published online: 29 June 2020

References

1. Ali, S. H. et al. Mineral supply for sustainable development requires resource governance. *Nature* **543**, 367–372 (2017).
2. Schodde, R. Long term trends in global exploration – are we finding enough metal? In *11th Fennoscandian Exploration and Mining Conference* (Minex Consulting, 2017); https://go.nature.com/3hfWBKo.
3. Nassar, N. T., Graedel, T. E. & Harper, E. M. By-product metals are technologically essential but have problematic supply. *Sci. Adv.* **1**, 1400180 (2015).
4. Mudd, G. M. et al. *Critical Minerals in Australia: a Review of Opportunities and Research Needs* (Geoscience Australia, 2018).
5. *Global Energy Transformation: a Roadmap to 2050* (IRENA, 2019).
6. Dominish, E., Teske, S. & Florin, N. *Responsible Minerals Sourcing for Renewable Energy* (UTS Institute for Sustainable Futures, 2019).
7. Sovacool, B. B. K. et al. Sustainable minerals and metals for a low-carbon future. *Science* **367**, 30–33 (2020).
8. The UNCOVER Group *Searching the deep Earth: A vision for exploration geoscience in Australia* (Australian Academy of Science, 2012).
9. McCuaig, T. C., Beresford, S. & Hronsky, J. Translating the mineral systems approach into an effective exploration targeting system. *Ore Geol. Rev.* **38**, 128–138 (2010).
10. Wyborn, L. A. I., Heinrich, C. A. & Jaques, A. L. Australian Proterozoic mineral systems: essential ingredients and mappable criteria. In *Proc. AusIMM Annual Conference*, 109–115 (Australasian Institute of Mining and Metallurgy, 1994).
11. Bierlein, F. P., Groves, D. I., Goldfarb, R. J. & Dubé, B. Lithospheric controls on the formation of provinces hosting giant orogenic gold deposits. *Miner. Depos.* **40**, 874–886 (2006).
12. McCuaig, T. C. & Hronsky, J. M. A. in *Building Exploration Capability for the 21st Century* Special Publication No. 18 (eds Kelley, K. D. & Golden, H. C.) 153–175 (Society of Economic Geologists, 2014).
13. Dentith, M., Yuan, H., Johnson, S., Murdie, R. & Piña-Varas, P. Application of deep-penetrating geophysical methods to mineral exploration: examples from western Australia. *Geophysics* **83**, https://doi.org/10.1190/geo2017-0482.1 (2018).
14. Skirrow, R. G. et al. Mapping iron oxide Cu–Au (IOCG) mineral potential in Australia using a knowledge-driven mineral systems-based approach. *Ore Geol. Rev.* **113**, 103011 (2019).
15. Begg, G. C. et al. Lithospheric, cratonic, and geodynamic setting of Ni–Cu–PGE sulfide deposits. *Econ. Geol.* **105**, 1057–1070 (2010).
16. Griffin, W. L., Begg, G. C. & O'Reilly, S. Y. Continental-root control on the genesis of magmatic ore deposits. *Nat. Geosci.* **6**, 905–910 (2013).

17. Rosenbaum, G. et al. Subduction of the Nazca Ridge and the Inca Plateau: insights into the formation of ore deposits in Peru. *Earth Planet. Sci. Lett.* **239**, 18–32 (2005).
18. Butterworth, N. et al. Tectonic environments of South American porphyry copper magmatism through time revealed by spatiotemporal data mining. *Tectonics* **35**, 2847–2862 (2016).
19. O'Reilly, S. Y., Griffin, W. L. & Pearson, N. J. Geodynamic and geophysical consequences of stealth(y) mantle metasomatism: Craton evolution and metallogeny. In *Proc. 11th International Kimberlite Conference* abstr. 4537 (2017).
20. McCuaig, T. C., Scarselli, S., Connor, T. O., Busuttil, S. & McCormack, N. in *Metals, Minerals, and Society* (eds Arribas R. et al.) Ch. 3 (Society of Economic Geologists, 2018).
21. Leach, D. L. et al. Sediment-hosted lead–zinc deposits in Earth history. *Econ. Geol.* **105**, 593–625 (2010).
22. Hitzman, M. W., Selley, D. & Bull, S. Formation of sedimentary rock-hosted stratiform copper deposits through Earth history. *Econ. Geol.* **105**, 627–639 (2010).
23. Manning, A. H. & Emsbo, P. Testing the potential role of brine reflux in the formation of sedimentary exhalative (sedex) ore deposits. *Ore Geol. Rev.* **102**, 862–874 (2018).
24. Huston, D. L. et al. Tectono-metallogenic systems – the place of mineral systems within tectonic evolution, with an emphasis on Australian examples. *Ore Geol. Rev.* **76**, 168–210 (2016).
25. Azadi, M., Northey, S. A., Ali, S. H. & Edraki, M. Transparency on greenhouse gas emissions from mining to enable climate change mitigation. *Nat. Geosci.* **13**, 100–104 (2020).
26. *Geophysical Archive Data Delivery System* (Geoscience Australia, 2018); geoscience.gov.au/gadds.
27. Priestley, K. & McKenzie, D. P. The relationship between shear wave velocity, temperature, attenuation and viscosity in the shallow part of the mantle. *Earth Planet. Sci. Lett.* **381**, 78–91 (2013).
28. Yamauchi, H. & Takei, Y. Polycrystal anelasticity at near-solidus temperatures. *J. Geophys. Res. Solid Earth* **121**, 7790–7820 (2016).
29. Fishwick, S. & Rawlinson, N. 3-D structure of the Australian lithosphere from evolving seismic datasets. *Aust. J. Earth Sci.* **59**, 809–826 (2012).
30. Schaeffer, A. J. & Lebedev, S. Global shear speed structure of the upper mantle and transition zone. *Geophys. J. Int.* **194**, 417–449 (2013).
31. Richards, F. D., Hoggard, M. J., Cowton, L. R. & White, N. J. Reassessing the thermal structure of oceanic lithosphere with revised global inventories of basement depths and heat flow measurements. *J. Geophys. Res. Solid Earth* **123**, 9136–9161 (2018).
32. Huston, D. L. et al. *Preliminary National-scale Lead Isotope Maps of Australia* Record 2019/01 (Geoscience Australia, 2019).
33. Hobbs, B. E. et al. in *After 2000 – the Future of Mining*, 34–49 (Australasian Institute of Mining and Metallurgy, 2000).
34. Kennett, B. L. N., Saygin, E., Fomin, T. & Blewett, R. *Deep Crustal Seismic Reflection Profiling: Australia 1978–2015* (ANU Press and Geoscience Australia, 2016).
35. Heinson, G., Didana, Y., Soeffky, P., Thiel, S. & Wise, T. The crustal geophysical signature of a world-class magmatic mineral system. *Sci. Rep.* **8**, 10608 (2018).
36. Skirrow, R. G., van der Wielen, S. E., Champion, D. C., Czarnota, K. & Thiel, S. Lithospheric architecture and mantle metasomatism linked to Iron Oxide Cu–Au ore formation: multidisciplinary evidence from the Olympic Dam region, South Australia. *Geochem. Geophys. Geosyst.* **19**, 2673–2705 (2018).
37. Curtis, S. & Thiel, S. Identifying lithospheric boundaries using magnetotellurics and Nd isotope geochemistry: an example from the Gawler Craton, Australia. *Precambrian Res.* **320**, 403–423 (2019).
38. Kolmogorov, A. N. Sulla determinazione empirica di una legge di distribuzione. *G. della Istituto Ital. degli Attuari* **4**, 83–91 (1933).
39. Menzies, M., Xu, Y., Zhang, H. & Fan, W. Integration of geology, geophysics and geochemistry: a key to understanding the North China craton. *Lithos* **96**, 1–21 (2007).
40. Currie, C. A. & van Wijk, J. How craton margins are preserved: insights from geodynamic models. *J. Geodyn.* **100**, 144–158 (2016).
41. Davies, D. R. & Rawlinson, N. On the origin of recent intraplate volcanism in Australia. *Geology* **42**, 1031–1034 (2014).
42. Sloan, R. A., Jackson, J. A., McKenzie, D. P. & Priestley, K. Earthquake depth distributions in central Asia, and their relations with lithosphere thickness, shortening and extension. *Geophys. J. Int.* **185**, 1–29 (2011).
43. Gibson, G. M. et al. Basin architecture and evolution in the Mount Isa mineral province, northern Australia: constraints from deep seismic reflection profiling and implications for ore genesis. *Ore Geol. Rev.* **76**, 414–441 (2016).
44. Biggs, J., Nissen, E., Craig, T., Jackson, J. & Robinson, D. P. Breaking up the hanging wall of a rift-border fault: the 2009 Karonga earthquakes, Malawi. *Geophys. Res. Lett.* **37**, L11305 (2010).
45. Allen, P. A. & Armitage, J. J. in *Tectonics of Sedimentary Basins: Recent Advances* 1st edn (eds Busby, C. and Azor, A.) Ch. 30 (Blackwell, 2012).
46. Jordan, T. H. Composition and development of the continental tectosphere. *Nature* **274**, 544–548 (1978).
47. Huston, D. L., Pehrsson, S., Eglington, B. M. & Zaw, K. The geology and metallogeny of volcanic-hosted massive sulfide deposits: variations through geologic time and with tectonic setting. *Econ. Geol.* **105**, 571–591 (2010).
48. Regis, D. et al. Evidence for Neoarchean Ni–Cu-bearing mafic intrusions along a major lithospheric structure: a case study from the south Rae craton (Canada). *Precambrian Res.* **302**, 312–339 (2017).
49. Alghamdi, A. H., Aitken, A. R. & Dentith, M. C. The deep crustal structure of the Warakurna LIP, and insights on Proterozoic LIP processes and mineralisation. *Gondwana Res.* **56**, 1–11 (2018).
50. Arndt, N. T., Lesher, C. M. & Czamanske, G. K. in *Economic Geology: 100th Anniversary Volume 1905–2005* (eds Hedenquist, J. W. et al.) 5–24 (Society of Economic Geologists, 2005).
51. Raymond, O., Totterdell, J. M., Woods, M. A. & Stewart, A. J. *Australian Geological Provinces 2018.01 edition* (Geoscience Australia, 2018); http://pid.geoscience.gov.au/dataset/ga/116823.

Methods

Deposit compilation. Our global inventory of 2,166 major base metal deposits are categorized into six main classes. Three are sediment hosted: Cu-sed (contains ~20% of all known copper), PbZn-CD (~43% of all lead and ~33% of zinc) and PbZn-MVT (~25% lead, ~22% zinc). The other three are associated with magmatic systems: copper porphyry (Cu-por; contains ~65% of all known copper) magmatic nickel–copper–platinum group elements (Ni-Cu-PGE; ~45% nickel, ~3% copper); and volcanogenic massive sulfides (VMS; ~6% copper, ~23% lead, ~39% zinc).

For each deposit, we include the type (on the basis of established classification schemes), location, age (direct measurement or inferred on the basis of geological relationships) and total resource size by combining historical production with estimated resources. Our Cu-sed deposit dataset follows the classification scheme and compilation of Hitzman et al., cross-checked against Cox et al.[52,53]. Where these two compilations disagree on deposit size, the larger value has been used. Our PbZn-CD and PbZn-MVT deposit compilations extensively revise and build on the work of Taylor et al.[54]. References for each deposit type were manually checked, and additional references have been included. We exploit the compilation of Sillitoe for Cu-por deposits[55]. Our magmatic Ni-Cu-PGE compilation follows Hoatson et al., with deposit location populated from disparate sources[56]. Our catalogue of VMS deposits is an extensive revision of the compilation by Franklin et al.[57]. Australian information for all these deposit types, with the addition of 25 IOCG deposits, was updated using the authors' own knowledge building from the Geoscience Australia **OZMin** database [58].

We have endeavoured to assemble the most complete deposit dataset possible by revising and extending pre-existing compilations. Our database can be found in the online Supplementary Datasets. Importantly, patchy or absent reporting of mineral deposit information from some countries inevitably means our global database is incomplete, but we do not believe that this will impact the veracity of our main conclusions.

Metal scavenging window. Following Cooke et al.[59], we have selected a precipitation gradient from ~100 ppm to 1 ppm for the metal-scavenging window in Fig. 1. Estimates of the metal concentration of mineralizing brines are obtained from fluid inclusion studies contained within ore and other gangue minerals. Care must be taken that host minerals formed during the period of ore deposition and that analyses are not contaminated by metals contained within the mineral lattice itself, which is a particular problem in the early stages of laser-ablation inductively coupled plasma-mass spectrometry, when the laser initially vaporizes a mixture of mineral and fluid inclusion to produce a mixed signal. Generally, inclusions from European sediment-hosted deposits and Irish and US MVTs hosted by quartz, calcite and dolomite have values at the lower end of our range, while those in sphalerite can sometimes reach several hundred ppm of Pb[60–64]. Values in the several thousands of ppm have been inferred in rare cases for single fluid inclusions[65,66]. However, these high values are often found for inclusions with high homogenization temperatures, while those fluids thought to be cooler than ~250 °C generally return concentrations an order of magnitude or more below 1,000 ppm[66]. While there remains debate on the complexity and exact composition of mineralizing fluids[67,68], for ores deposited via the reduction mechanism, our inference of an enlarged operating window in cratonic rift basins holds regardless of the exact fluid metal concentrations.

Choice of seismic tomography model. Our LAB maps are based on recent shear-wave velocity (V_S) models that contain a lot of surface-wave data and have nominal vertical resolution on the order of 25–50 km[69]. For the global map, we use **SL2013sv**[30], which is an upper-mantle-only model built from a combination of body and surface waves, including fundamental and higher modes. Periods considered are 11–450 s, ~750,000 seismograms are included and misfits are calculated between synthetics and the full waveform up to the 18th overtone. Crucially, simultaneous inversion for the crustal model results in reduced smearing of slow crustal velocities down into the upper mantle compared with other models, thereby allowing us to use more depth slices in our shear-wave velocity to temperature calibration. Chequerboard resolution tests indicate that features ~600 km in diameter at lithospheric depths are generally well resolved. Finer features should be resolvable in regions with dense ray path coverage, such as North America, Europe and Southeast Asia. The **SL2013sv** model uses data from only six seismometers in Australia, so it has limited resolution within this continent. Therefore, we also investigate the **FR12** regional seismic tomography model[29] to generate a high-resolution map for the Australian continent. **FR12** is a radially isotropic V_S model derived from Rayleigh wave travel times[70]. Periods considered are 50–120 s and the fundamental and first four higher modes have been used where possible, leading to good sensitivity down to ~250-km depths. It contains a greater number of source–receiver paths (>13, 000) compared with other Australian models. However, it uses an a priori crustal model that remains fixed throughout the inversion, resulting in noticeable smearing of crustal velocities into the upper mantle. Chequerboard tests indicate that features ~300 km in diameter at lithospheric depths are well resolved, and where higher mode information is included.

For comparison, we include LAB maps derived from three additional upper-mantle seismic tomography datasets with global coverage in Extended Data Fig. 1. These include the **3D2015-07Sv** model[71], the **CAM2016** model[72,73] and a version of **SL2013sv** into which we have blended the regional updates **SL2013NA** in North America[74], **AF2019** in Africa[75] and **SA2019** in South America and the South Atlantic Ocean[76] to produce a combined model **SLNAAFSA**. For the continental analyses in Australia, we also consider regional models **AuSREM**[77] and **Y14**[78]. Deposit locations are compared with all 7 of our new LAB maps in the Supplementary Information, in addition to 11 previously published LAB maps derived from a mixture of heat flow data, seismic tomography datasets and potential field data. Many giant sediment-hosted mineral deposits lie along LAB edges defined by these other studies, testifying to the robustness of the observed relationship.

Parameterizing anelasticity. Seismic tomography models provide images of the upper mantle and have been extensively used to constrain its thermomechanical structure, its composition and the depth of the LAB[69,79–84]. For accurate mapping from V_S into temperature, it is essential to include the effect of anelasticity on this conversion[85,86]. When a viscoelastic material such as the mantle is cold, deformation associated with passage of acoustic energy is predominantly elastic, yielding a linear dependence of V_S on temperature referred to as the anharmonic velocity. As temperature increases, a special case of viscoelastic deformation known as anelasticity becomes increasingly important and gives rise to a strongly nonlinear relationship between V_S and temperature. This behaviour has been extensively studied in laboratory experiments on silicates and organic analogues of mantle rocks, revealing that the strength of the anelastic regime varies with both the frequency of seismic waves and as a function of material properties, such as melting temperature and grain size[87–91]. Several studies have attempted to parameterize these complex dependencies and have been regularly updated as forced oscillation and creep experiments in the laboratory have been pushed towards increasingly realistic frequencies, pressures, temperatures, grain sizes and strain rates[92–94]. In this study, we adopt the parameterization of Yamauchi and Takei[28], which includes effects of anelasticity in pre-melt conditions (temperatures above ~90% of melting temperature) and is outlined in full in the Supplementary Information.

Xenolith and xenocryst thermobarometry. Temperature estimates across a range of depths are required to generate a series of V_S–temperature–pressure tie points to calibrate the regional seismic tomography models. We therefore assemble a suite of 15 Australian palaeogeotherms derived from thermobarometric analysis of mantle xenoliths and xenocrysts (Supplementary Information). These come from a range of settings within both thick and thin lithosphere. Localities with thin lithosphere tend to have data obtained from whole xenolith samples, typically hosted in basaltic volcanic products. For these cases, the compositions of multiple phases (garnet, clinopyroxene, orthopyroxene and olivine) can be obtained that all equilibrated under the same pressure–temperature (P–T) conditions. In these samples, we use a thermometer[95] that exploits exchange of calcium and magnesium between orthopyroxene and clinopyroxene and a barometer[96] that uses aluminium exchange between orthopyroxene and garnet, given by equation (5) of Nickel and Green[96]. This approach therefore requires compositions of garnet, diopside (clinopyroxene) and enstatite (orthopyroxene) for each xenolith, and we only use samples with all three of these minerals present. This barometer and thermometer pair also depend on the temperature and pressure, respectively. These two equations are therefore solved simultaneously by iteration to obtain equilibration P–T conditions. Samples are discarded if they fail more than one of the eight oxide, cation and equilibration checks [97].

Despite all samples containing garnet, a small number return depths as shallow as ~25 km (see Bullenmerri, Monaro, Mt. St. Martin and Sapphire Hill). The presence of garnet in xenoliths from shallow depths is well documented. The garnet–spinel transition can occur at pressures as low as 1 GPa (~30 km depth) in pyroxenite and 1.5 GPa (~45 km depth) in lherzolite, with the exact pressure of the transition depending on the relative abundance of Cr and Al in each assemblage[97–99]. Our shallow samples are dominantly pyroxenites and mostly give pressures larger than the 1 GPa lower limit. Of these four sites with shallower samples, we select only Bullenmerri and Monaro for the anelasticity calibration as these geotherms also contain samples at greater depths. In both cases, the deeper samples are consistent with the shallow results.

Analyses from locations on thicker lithosphere are obtained predominantly from heavy mineral concentrates generated during diamond exploration (plus rare diamond inclusions and occasional whole peridotite xenoliths), where the association of one mineral grain with any other has been lost. Thus, the approach outlined in the preceding paragraphs using multiple phases is unavailable, and we instead turn to single-grain combined thermobarometers for deriving equilibration P–T conditions. For these samples, we use the chrome-in-diopside barometer that exploits the exchange of chromium between clinopyroxene and garnet (equation (9) of Nimis and Taylor)[100]. It uses only diopside compositions but requires that garnet was also present in the source region. The associated thermometer exploits enstatite-in-diopside, again using only diopside compositions but requiring that orthopyroxene was present within the source. The temperature is given by equation (17) of Nimis and Taylor[100]. Again, these two equations must be solved by iteration to obtain P–T conditions for each diopside grain. Calibration on laboratory

experiments has shown that this thermobarometer may become inaccurate at low pressures and at temperatures <700 °C[97]. We therefore use only *P–T* estimates derived from this thermobarometer that yield depths >60 km and pass both of the clinopyroxene cation and oxide checks.

There are two sources of error to consider for each suite of *P–T* estimates. The first is uncertainty in the microprobe analyses of elemental oxide concentrations in each of the mineral samples. For the three-mineral thermobarometer, this introduces uncertainty of ±30 °C and ±10 km at low temperatures (~700 °C), reducing to ±10 °C and ±3 km by ~1,200 °C[101]. For the diopside-only thermobarometer, uncertainties are larger at ±70 °C and ±12 km for low temperatures (~600 °C) and ±15 °C and ±3 km for higher temperatures (~1,200 °C)[101]. However, these uncertainties in pressure and temperature are positively correlated, such that samples broadly move up and down the geothermal gradient, with limited effect on the best-fitting geotherm. The second and more significant source of uncertainty arises from error in the thermobarometers themselves, which are calibrated on laboratory samples over a range of *P–T* conditions and do not necessarily trade off in the same manner. Quoted uncertainties are ±50 °C and ±15 km for the three-mineral thermobarometer and ±100 °C and ±15 km for the diopside-only thermobarometer [97,100,101].

Fitting a geotherm to *P–T* estimates. For each locality, *P–T* estimates derived from thermobarometry are entered into **FITPLOT**[101,102] to constrain the best-fitting palaeogeotherm (Supplementary Information). Within the crust, we adopt a constant conductivity of 2.5 W m^{-1} °C^{-1}, while a pressure- and temperature-dependent parameterization is used within the mantle[103]. Bulk crustal radiogenic heat production is assumed to be 0.7 μW m^{-3}, with standard deviation (s.d.) of 0.2 μW m^{-3}[104]. Crustal thickness at each location is obtained from the **AusMoho** model[105] with s.d. assigned as 10% of the total thickness. We assume a potential temperature of 1,330 ± 50 °C, which is consistent with both seismological observations and the thickness and geochemistry of mid-ocean-ridge basalts, assuming a dry lherzolite source using a corner-flow melting parameterization[106–108]. Kinematic viscosity of the mantle is set to 2×10^{16} m^2 s^{-1}, with s.d. of 0.7 orders of magnitude, which is consistent with constraints from glacial isostatic adjustment[109]. Thermal parameters that are consistent with the melting parameterization are used to calculate the adiabatic gradient, including a reference density of $\rho_0 = 3.3$ Mg m^{-3}, thermal expansivity of $\alpha = 3\times10^{-5}$ °C^{-1} and specific heat capacity of $C_p = 1{,}187$ J kg^{-1} °C^{-1}. Uncertainty in the crustal thickness, radiogenic heat production, mantle potential temperature and kinematic viscosity are propagated through **FITPLOT** using a Monte Carlo approach. One thousand combinations of these four parameters are randomly drawn assuming Gaussian distributions of the uncertainties. Geotherms are strongly consistent in the vicinity of *P–T* constraints but can vary by ±50 °C when greater than ~30 km from a *P–T* estimate (Supplementary Information).

Calibrating V_S-to-temperature conversion. Some of the anelasticity parameters have been directly constrained by forced oscillation experiments on borneol[28]. However, others are material properties that must be independently determined. A widely adopted approach is to fix these parameters for a given mineral assemblage, often calculated using mineral physics tables and a thermodynamic Gibbs energy minimization algorithm[110–114]. In this manner, an anelastic conversion can be used in a forward sense to map between V_S and temperature[79,80,82,115,116]. However, inferred temperature structures are variable as a result of uncertainty in the mantle's chemical composition and grain size and differences in absolute V_S between tomography models arising from different reference models and regularization schemes.

An alternative approach to constraining these material properties is to invert real-Earth observations of the relationship among temperature, V_S, attenuation and viscosity in the upper mantle[28,69,117,118]. The general philosophy is that there are certain properties that are 'known' about Earth, including the typical thermal structure of oceanic lithosphere[31], the average adiabatic gradient within the convecting mantle[111], the attenuation structure of the upper mantle beneath old oceanic lithosphere[119] and the bulk diffusion creep viscosity of the upper mantle from studies of glacial isostatic adjustment[109]. Thus, any thermal model inferred from V_S should be compatible with these observations. This general approach was pioneered by Priestley and McKenzie[27,69]. The approach has been further refined by Richards et al.[120], and we adopt their approach for calibration of global tomography models (see Supplementary Information).

For the Australian regional tomography models, we cannot use oceanic observations for calibration due to insufficient offshore coverage, and instead use the better-constrained palaeogeotherms derived from thermobarometry on mantle xenoliths (in combination with the adiabatic gradient). Away from three close-together sites in South Australia in the vicinity of the Gawler Craton, it is notable that the global **SL2013sv** model provides a surprisingly good fit to the Australian palaeogeotherms, despite being calibrated independently (Supplementary Information). This observation is unexpected for two reasons. First, the nominal resolution of the global model is lower than that of the local models. There are only six seismometers in Australia (located in the far west, north and east of the continent, with none in South Australia), and the density of crossing ray paths is much lower than in Europe, Asia, North America and South America[30]. Second, the Australian geotherms occur in continental lithosphere that is thought to be chemically depleted by melt extraction, reducing the quantity of garnet and clinopyroxene with respect to more fertile oceanic mantle. Nevertheless, the global model calibrated on fertile mantle constraints provides a good match to independent V_S–*T*–*P* observations in depleted continental lithosphere. This result implies that temperature plays the dominant role in controlling variations in seismic wave speed in the shallow mantle, while the effects of compositional variation are substantially smaller [69,121,122].

Mapping the LAB. A recent study on the thermal structure of oceanic lithosphere found that the 1,175 ± 50 °C isotherm provides a good match to seismological observations of the LAB[31]. In this study, we therefore adopt this isotherm as a proxy for lithospheric thickness beneath the continents. The temperature (T) as a function of depth (z) is extracted from the V_S model and $\frac{\partial T}{\partial z}$ calculated over 25-km increments. Starting from the surface and progressing downwards, when temperature passes the 1,175 °C threshold, LAB depth is calculated using linear interpolation, with one important exception. In locations of thick crust, low V_S values at shallow depths arising from crustal bleeding can lead to lithospheric mantle being erroneously interpreted as hot. In the regional seismic tomography models, this crustal bleeding can be observed down to ~125 km in some locations (see calibration figure (Supplementary Fig. 7) in Supplementary Information). To circumvent this issue, when an inverted temperature gradient is found at shallow depths, we move on to deeper levels until temperature starts to increase with depth. This crustal bleeding is only considered down to 200 km. Maximum LAB depth is limited to 350 km or the deepest slice in the seismic tomography model. Our 1,175 °C isotherm LAB proxy is shallower than used in some other studies that define the LAB using the intersection of conductive and adiabatic temperature gradients in the thermal boundary layer[27,101] (typically occurring at temperatures 1,350–1,450 °C). However, in addition to matching oceanic observations, the 1,175 °C isotherm corresponds to lower homologous temperatures, where uncertainty in anelastic parameters has a smaller impact on the recovered LAB.

As in previous studies using seismic tomography[27,73,84,123], our LAB map exhibits regions of thick lithosphere in some subduction zones (for example, the west coast of South America, south Alaska and Japan). Many of these features are likely to represent subducting slabs rather than cratonic lithosphere. None of the giant (>10 Mt of contained metal) sediment-hosted deposits is found in these settings, although some minor sedimentary copper deposits do occur, particularly in the Andes. These deposits may well represent distal components of porphyry coppers, but we have left them in our sedimentary copper dataset in line with pre-existing classification schemes. It is possible to manually exclude potential slab-related features from the analysis using the **Slab2** model[124] (Supplementary Information). Doing so improves the results of statistical tests, with the chances of the relationship between sediment-hosted deposits and the edge of cratonic lithosphere being random reducing by a factor of three. This occurs because the continental area within 200 km of the 170-km LAB contour decreases from 34.3% to 31.0%, while only marginally increasing the proportion of small outlier deposits. Nevertheless, we have deliberately retained these regions in the main text to avoid introducing subjectivity and bias into our LAB maps, as opinions are likely to differ on which features to exclude. Furthermore, some studies argue that over long periods, thick lithosphere may be generated at subduction zones by thrust stacking[125]. Thus, exclusion of these features is potentially unwarranted.

Test suites of random continental locations. To test the statistical significance of real deposit locations, a test suite of random points on a sphere have been generated by randomly selecting two variables, a and b, in the range 0–1 and converting into longitude, θ, and latitude, ϕ, using area-normalized relationships

$$\theta = 360\times a \tag{1}$$

$$\phi = \frac{180}{\pi}\times \arcsin(2b-1) \tag{2}$$

These are subsequently filtered to select only those points that lie onshore (Supplementary Information). For each location, the closest approach to the 170-km lithospheric thickness contour is calculated, and the resulting distances are plotted in a CDF.

Kolmogorov–Smirnov statistical tests. We use the two-sample Kolmogorov–Smirnov test to examine whether the difference between two cumulative distribution functions is significant, given their respective population sizes. The D value is the maximum magnitude of the difference between two CDFs at any point[38]. The test calculates the probability that a D value of this magnitude might accidentally occur, had the two CDFs been randomly selected from the same underlying population. The probability, Pr, is approximated using

$$\Pr \approx \exp\left(\frac{-2pqD^2}{p+q}\right) \tag{3}$$

where p and q are the number of samples in each CDF and D is the D value expressed as a fraction between 0 and 1. For each Kolmogorov–Smirnov test,

a number of random points is generated that is equivalent to the number of real deposits of that type (109 for PbZn-CD, 147 for PbZn-MVT and 139 for sedimentary copper). Given the low sample size for some of the deposit classes, the distribution of this random set can vary somewhat from the true average distribution of random continental locations. We therefore draw a test set in this manner 100 times and report the Kolmogorov–Smirnov statistics associated with each separate test within a histogram. For PbZn-CD deposits, the D value between the real non-weighted, regionally enhanced CDF and each random CDF is individually calculated, yielding a mean and s.d. of $D = 0.36 \pm 0.05$, with extremes of 0.26–0.46. For the combined sediment-hosted deposits in Fig. 3, the equivalent values are $D = 0.27 \pm 0.02$ with extremes of 0.22–0.32. A D value of 0.27 for the 395 combined sedimentary-hosted deposits suggests that the probability this CDF is drawn from randomly distributed continental points is less than 1 in 10^{12} (Supplementary Information).

Thermal modelling of lithospheric rifting. Rifting of continental lithosphere causes subsidence of the surface to form a basin that progressively infills with sediments. An initial syn-rift subsidence phase occurs during lateral extension and vertical thinning of the crust and lithospheric mantle, which is contemporaneous with normal faulting. Following cessation of extension, faulting stops and post-rift thermal subsidence occurs as hot, upwelled asthenospheric mantle conductively cools back to an equilibrium lithospheric thickness[126]. To predict the subsidence and basal heat flow of the basin, we model the one-dimensional thermal evolution of the lithosphere during rifting using a finite difference scheme. Following McKenzie[126], we assume thinning occurs by pure shear and that vertical heat transfer dominates.

For each rift scenario, we select an initial lithospheric template. For regular continental lithosphere, the crustal thickness is set to 30 km and the total lithospheric thickness to 140 km, which matches results from plate cooling models of oceanic lithosphere[31] and places the 1,175 °C isotherm at ~120 km. Radiogenic heat production in the mantle is set to zero, while the crustal value is tuned to 1.0 μW m^{-3} such that the steady-state geotherm yields a surface heat flow of ~63 mW m^{-2}, which is the average for Phanerozoic continental lithosphere[127]. For cratonic lithosphere, we assume an initial crustal thickness of 50 km, lithospheric thickness of 280 km (1,175 °C isotherm at ~240 km) and crustal radiogenic heat production of 0.57 μW m^{-3}, which yields an initial surface heat flux consistent with the average of ~48 mW m^{-2} for Archaean and cratonic areas[127]. On the basis of the typically low palaeowater depth of sediments found in proximal portions of these basins and the high supply of clastic material from adjacent cratons, we assume the basin is constantly filled by sediments. We subsequently predict the temperature of the sediment pile using the basal heat flux and a constant sediment conductivity of 2.5 W m^{-1} K^{-1}, assuming a steady-state conductive geotherm and negligible internal heat generation. Details of the finite difference scheme, thermal parameterizations and individual model runs are given in the Supplementary Information.

Data availability

All data, including digital versions of lithospheric thickness maps and deposit databases, are available in the manuscript or the Supplementary Information, and on the OSF database (https://osf.io/twksd).

References

52. Hitzman, M. W., Kirkham, R., Broughton, D., Thorson, J. & Selley, D. in *Economic Geology: 100th Anniversary Volume 1905–2005* (eds Hedenquist, J. W. et al.) 609–642 (Society of Economic Geologists, 2005).
53. Cox, D. P., Lindsey, D. A., Singer, D. A., Moring, B. C. & Diggles, M. F. *Sediment-hosted Copper Deposits of the World: Deposit Models and Database* Open-File Report 03-107 (USGS, 2007).
54. Taylor, R. D., Leach, D. L., Bradley, D. C. & Pisarevsky, S. A. *Compilation of Mineral Resource Data for Mississippi Valley-type and Clastic-dominated Sediment-hosted Lead-Zinc Deposits* Open-File Report 1297 (USGS, 2009).
55. Sillitoe, R. H. Porphyry copper systems. *Econ. Geol.* **105**, 3–41 (2010).
56. Hoatson, D. M., Jaireth, S. & Jaques, A. L. Nickel sulfide deposits in Australia: characteristics, resources, and potential. *Ore Geol. Rev.* **29**, 177–241 (2006).
57. Franklin, J. M., Gibson, H. L., Jonasson, I. R. & Galley, A. G. in *Economic Geology: 100th Anniversary Volume 1905–2005* (eds Hedenquist, J. W. et al.) 523–560 (Society of Economic Geologists, 2005).
58. Sexton, M. *Australian Mineral Occurrences Collection* eCat Id 73131 (Geoscience Australia, 2011); http://pid.geoscience.gov.au/dataset/ga/73131.
59. Cooke, D. R., Bull, S. W., Large, R. R. & McGoldrick, P. J. The importance of oxidized brines for the formation of Australian Proterozoic stratiform sediment-hosted Pb–Zn (sedex) deposits. *Econ. Geol.* **95**, 1–18 (2000).
60. Appold, M. S., Numelin, T. J., Shepherd, T. J. & Chenery, S. R. Limits on the metal content of fluid inclusions in gangue minerals from the Viburnum Trend, Southeast Missouri, determined by laser ablation ICP-MS. *Econ. Geol.* **99**, 185–198 (2004).
61. Kostova, B., Pettke, T., Driesner, T., Petrov, P. & Heinrich, C. A. LA ICP-MS study of fluid inclusions in quartz from the Yuzhna Petrovitsa deposit, Madan ore field, Bulgaria. *Swiss Bull. Mineral. Petrol.* **84**, 25–36 (2004).
62. Wilkinson, J. J., Everett, C. E., Boyce, A. J., Gleeson, S. A. & Rye, D. M. Intracratonic crustal seawater circulation and the genesis of subseafloor zinc–lead mineralization in the Irish orefield. *Geology* **33**, 805–808 (2005).
63. Kotzeva, B. G., Guillong, M., Stefanova, E. & Piperov, N. B. LA-ICP-MS analysis of single fluid inclusions in a quartz crystal (Madan ore district, Bulgaria). *J. Geochem. Explor.* **108**, 163–175 (2011).
64. Fusswinkel, T., Wagner, T., Wenzel, T., Wälle, M. & Lorenz, J. Red bed and basement sourced fluids recorded in hydrothermal Mn–Fe–As veins, Sailauf (Germany): a LA-ICPMS fluid inclusion study. *Chem. Geol.* **363**, 22–39 (2014).
65. Wilkinson, J. J., Stoffell, B., Wilkinson, C. C., Jeffries, T. E. & Appold, M. S. Anomalously metal-rich fluids form hydrothermal ore deposits. *Science* **323**, 764–767 (2009).
66. Davey, J. *Anomalous Metal Enrichment of Basin Brines in the Zambian Copperbelt: a Comparison of Fluid Chemistry in Contrasting Sediment-hosted Copper Systems*. PhD thesis, Univ. Southampton (2019).
67. Fusswinkel, T. et al. Fluid mixing forms basement-hosted Pb–Zn deposits: insight from metal and halogen geochemistry of individual fluid inclusions. *Geology* **41**, 679–682 (2013).
68. Schlegel, T. U., Wagner, T., Wälle, M. & Heinrich, C. A. Hematite breccia-hosted iron oxide copper–gold deposits require magmatic fluid components exposed to atmospheric oxidation: evidence from Prominent Hill, Gawler Craton, South Australia. *Econ. Geol.* **113**, 597–644 (2018).
69. Priestley, K. & McKenzie, D. P. The thermal structure of the lithosphere from shear wave velocities. *Earth Planet. Sci. Lett.* **244**, 285–301 (2006).
70. Fishwick, S., Heintz, M., Kennett, B. L. N., Reading, A. M. & Yoshizawa, K. Steps in lithospheric thickness within eastern Australia, evidence from surface wave tomography. *Tectonics* **27**, TC4009 (2008).
71. Debayle, E., Dubuffet, F. & Durand, S. An automatically updated S-wave model of the upper mantle and the depth extent of azimuthal anisotropy. *Geophys. Res. Lett.* **43**, 674–682 (2016).
72. Ho, T., Priestley, K. & Debayle, E. A global horizontal shear velocity model of the upper mantle from multimode Love wave measurements. *Geophys. J. Int.* **207**, 542–561 (2016).
73. Priestley, K., McKenzie, D. & Ho, T. in *Lithospheric Discontinuities* (eds Yuan, H. and Romanowicz, B.) Ch. 6 (Wiley, 2018).
74. Schaeffer, A. J. & Lebedev, S. Imaging the North American continent using waveform inversion of global and USArray data. *Earth Planet. Sci. Lett.* **402**, 26–41 (2014).
75. Celli, N. L., Lebedev, S., Schaeffer, A. J. & Gaina, C. African cratonic lithosphere carved by mantle plumes. *Nat. Commun.* **11**, 92 (2020).
76. Celli, N. L., Lebedev, S., Schaeffer, A. J., Ravenna, M. & Gaina, C. The upper mantle beneath the South Atlantic Ocean, South America and Africa from waveform tomography with massive data sets. *Geophys. J. Int.* **221**, 178–204 (2020).
77. Kennett, B. L. N., Fichtner, A., Fishwick, S. & Yoshizawa, K. Australian seismological reference model (AuSREM): mantle component. *Geophys. J. Int.* **192**, 871–887 (2013).
78. Yoshizawa, K. Radially anisotropic 3-D shear wave structure of the Australian lithosphere and asthenosphere from multi-mode surface waves. *Phys. Earth Planet. Inter.* **235**, 33–48 (2014).
79. An, M. & Shi, Y. Lithospheric thickness of the Chinese continent. *Phys. Earth Planet. Inter.* **159**, 257–266 (2006).
80. Goes, S., Armitage, J., Harmon, N., Smith, H. & Huismans, R. Low seismic velocities below mid-ocean ridges: attenuation versus melt retention. *J. Geophys. Res.* **117**, B12403 (2012).
81. Afonso, J. C. et al. 3-D multiobservable probabilistic inversion for the compositional and thermal structure of the lithosphere and upper mantle: III. Thermochemical tomography in the Western-Central US. *J. Geophys. Res. Solid Earth* **121**, 7337–7370 (2016).
82. Cammarano, F. & Guerri, M. Global thermal models of the lithosphere. *Geophys. J. Int.* **210**, 56–72 (2017).
83. Klöcking, M., White, N. J., Maclennan, J., McKenzie, D. & Fitton, J. G. Quantitative relationships between basalt geochemistry, shear wave velocity, and asthenospheric temperature beneath western North America. *Geochem. Geophys. Geosyst.* **19**, 3376–3404 (2018).
84. Afonso, J. C., Salajegheh, F., Szwillus, W., Ebbing, J. & Gaina, C. A global reference model of the lithosphere and upper mantle from joint inversion and analysis of multiple data sets. *Geophys. J. Int.* **217**, 1602–1628 (2019).
85. Karato, S. Importance of anelasticity in the interpretation of seismic tomography. *Geophys. Res. Lett.* **20**, 1623–1626 (1993).
86. Cammarano, F., Goes, S., Vacher, P. & Giardini, D. Inferring upper-mantle temperatures from seismic velocities. *Phys. Earth Planet. Inter.* **138**, 197–222 (2003).
87. Jackson, I., FitzGerald, J. D., Faul, U. H. & Tan, B. H. Grain-size-sensitive seismic wave attenuation in polycrystalline olivine. *J. Geophys. Res.* **107**, 2360 (2002).
88. Sundberg, M. & Cooper, R. F. A composite viscoelastic model for incorporating grain boundary sliding and transient diffusion creep:

correlating creep and attenuation responses for materials with a fine grain size. *Phil. Mag.* **90**, 2817–2840 (2010).
89. McCarthy, C., Takei, Y. & Hiraga, T. Experimental study of attenuation and dispersion over a broad frequency range: 2. The universal scaling of polycrystalline materials. *J. Geophys. Res.* **116**, B09207 (2011).
90. Takei, Y., Karasawa, F. & Yamauchi, H. Temperature, grain size, and chemical controls on polycrystal anelasticity over a broad frequency range extending into the seismic range. *J. Geophys. Res. Solid Earth* **119**, 5414–5443 (2014).
91. Faul, U. & Jackson, I. Transient creep and strain energy dissipation: an experimental perspective. *Annu. Rev. Earth Planet. Sci.* **43**, 541–569 (2015).
92. Faul, U. H. & Jackson, I. The seismological signature of temperature and grain size variations in the upper mantle. *Earth Planet. Sci. Lett.* **234**, 119–134 (2005).
93. Jackson, I. & Faul, U. H. Grainsize-sensitive viscoelastic relaxation in olivine: towards a robust laboratory-based model for seismological application. *Phys. Earth Planet. Inter.* **183**, 151–163 (2010).
94. Takei, Y. Effects of partial melting on seismic velocity and attenuation: a new insight from experiments. *Annu. Rev. Earth Planet. Sci.* **45**, 447–470 (2017).
95. Taylor, W. R. An experimental test of some geothermometer and geobarometer formulations for upper mantle peridotites with application to the thermobarometry of fertile lherzolite and garnet websterite. *J. Mineral. Geochem.* **172**, 381–408 (1998).
96. Nickel, K. G. & Green, D. H. Empirical geothermobarometry for garnet peridotites and implications for the nature of the lithosphere, kimberlites and diamonds. *Earth Planet. Sci. Lett.* **73**, 158–170 (1985).
97. Nimis, P. & Grütter, H. Internally consistent geothermometers for garnet peridotites and pyroxenites. *Contrib. Mineral. Petrol.* **159**, 411–427 (2010).
98. Gasparik, T. Two-pyroxene thermobarometry with new experimental data in the system $CaO–MgO–Al_2O_3–SiO_2$. *Contrib. Mineral. Petrol.* **87**, 87–97 (1984).
99. Klemme, S. The influence of Cr on the garnet–spinel transition in the Earth's mantle: experiments in the system $MgO–Cr_2O_3–SiO_2$ and thermodynamic modelling. *Lithos* **77**, 639–646 (2004).
100. Nimis, P. & Taylor, W. R. Single clinopyroxene thermobarometry for garnet peridotites. Part I. Calibration and testing of a Cr-in-Cpx barometer and an enstatite-in-Cpx thermometer. *Contrib. Mineral. Petrol.* **139**, 541–554 (2000).
101. Mather, K. A., Pearson, D. G., McKenzie, D. P., Kjarsgaard, B. A. & Priestley, K. Constraints on the depth and thermal history of cratonic lithosphere from peridotite xenoliths, xenocrysts and seismology. *Lithos* **125**, 729–742 (2011).
102. McKenzie, D. P., Jackson, J. & Priestley, K. Thermal structure of oceanic and continental lithosphere. *Earth Planet. Sci. Lett.* **233**, 337–349 (2005).
103. Osako, M., Ito, E. & Yoneda, A. Simultaneous measurements of thermal conductivity and thermal diffusivity for garnet and olivine under high pressure. *Phys. Earth Planet. Inter.* **143–144**, 311–320 (2004).
104. Jaupart, C., Labrosse, S. & Mareschal, J. C. in *Treatise on Geophysics* Vol. 7 (eds Schubert, G. and Bercovici, D.) 253–303 (Elsevier, 2007).
105. Kennett, B. L. N., Salmon, M., Saygin, E. & Group, A. W. AusMoho: the variation of Moho depth in Australia. *Geophys. J. Int.* **187**, 946–958 (2011).
106. Dalton, C. A., Langmuir, C. H. & Gale, A. Geophysical and geochemical evidence for deep temperature variations beneath mid-ocean ridges. *Science* **344**, 80–83 (2014).
107. Katz, R. F., Spiegelman, M. & Langmuir, C. H. A new parameterization of hydrous mantle melting. *Geochem. Geophys. Geosyst.* **4**, 1073 (2003).
108. Shorttle, O., Maclennan, J. & Lambart, S. Quantifying lithological variability in the mantle. *Earth Planet. Sci. Lett.* **395**, 24–40 (2014).
109. Lau, H. C. et al. Inferences of mantle viscosity based on ice age data sets: radial structure. *J. Geophys. Res. Solid Earth* **121**, 6991–7012 (2016).
110. Stixrude, L. & Lithgow-Bertelloni, C. Thermodynamics of mantle minerals—I. Physical properties. *Geophys. J. Int.* **162**, 610–632 (2005).
111. Connolly, J. A. The geodynamic equation of state: what and how. *Geochem. Geophys. Geosyst.* **10**, Q10014 (2009).
112. Stixrude, L. & Lithgow-Bertelloni, C. Thermodynamics of mantle minerals—II. Phase equilibria. *Geophys. J. Int.* **184**, 1180–1213 (2011).
113. Holland, T. J. & Powell, R. An improved and extended internally consistent thermodynamic dataset for phases of petrological interest, involving a new equation of state for solids. *J. Metamorph. Geol.* **29**, 333–383 (2011).
114. Cottaar, S., Heister, T., Rose, I. & Unterborn, C. BurnMan: a lower mantle mineral physics toolkit. *Geochem. Geophys. Geosyst.* **15**, 1164–1179 (2014).
115. Cammarano, F., Romanowicz, B., Stixrude, L., Lithgow-bertelloni, C. & Xu, W. Inferring the thermochemical structure of the upper mantle from seismic data. *Geophys. J. Int.* **179**, 1169–1185 (2009).
116. Dannberg, J. et al. The importance of grain size to mantle dynamics and seismological observations. *Geochem. Geophys. Geosyst.* **18**, 3034–3061 (2017).
117. Afonso, J. C. et al. 3-D multiobservable probabilistic inversion for the compositional and thermal structure of the lithosphere and upper mantle. I: a priori petrological information and geophysical observables. *J. Geophys. Res. Solid Earth* **118**, 2586–2617 (2013).
118. Afonso, J. C., Fullea, J., Yang, Y., Connolly, J. A. & Jones, A. G. 3-D multi-observable probabilistic inversion for the compositional and thermal structure of the lithosphere and upper mantle. II: general methodology and resolution analysis. *J. Geophys. Res. Solid Earth* **118**, 1650–1676 (2013).
119. Dalton, C. A., Ekström, G. & Dziewonski, A. M. Global seismological shear velocity and attenuation: a comparison with experimental observations. *Earth Planet. Sci. Lett.* **284**, 65–75 (2009).
120. Richards, F. D., Hoggard, M. J., White, N. J. & Ghelichkhan, S. Quantifying the relationship between short-wavelength dynamic topography and thermomechanical structure of the upper mantle using calibrated parameterization of anelasticity. *J. Geophys. Res. Solid Earth* (in the press).
121. Goes, S., Govers, R. & Vacher, P. Shallow mantle temperatures under Europe from P and S wave tomography. *J. Geophys. Res.* **105**, 11153–11169 (2000).
122. Schutt, D. L. & Lesher, C. E. Effects of melt depletion on the density and seismic velocity of garnet and spinel lherzolite. *J. Geophys. Res.* **111**, B05401 (2006).
123. Steinberger, B. & Becker, T. W. A comparison of lithospheric thickness models. *Tectonophysics* **746**, 325–338 (2018).
124. Hayes, G. P. et al. Slab2, a comprehensive subduction zone geometry model. *Science* **362**, 58–61 (2018).
125. Cook, F. A., Van Der Velden, A. J., Hall, K. W. & Roberts, B. J. Frozen subduction in Canada's Northwest Territories: lithoprobe deep lithospheric reflection profiling of the western Canadian Shield. *Tectonics* **18**, 1–24 (1999).
126. McKenzie, D. P. Some remarks on the development of sedimentary basins. *Earth Planet. Sci. Lett.* **40**, 25–32 (1978).
127. Lucazeau, F. Analysis and mapping of an updated terrestrial heat flow data set. *Geochem. Geophys. Geosyst.* **20**, 4001–4024 (2019).

Acknowledgements

This work is a contribution to the Australian government's Exploring for the Future program. We are grateful to B. Steinberger, N. Rawlinson, K. Yoshizawa and B. Kennett for sharing lithospheric thickness maps. We thank J. C. Afonso, E. Bastrakov, G. Begg, R. Blewett, A. Bufe, D. Champion, R. Davies, B. Delbridge, A. Dickinson, M. Doublier, R. Fu, S. Goes, A. Gorbatov, B. Hodgin, B. Holtzman, C. Jiang, J. Kingslake, S. Liu, Z. Ma, T. Mackey, P. McFadden, D. McKenzie, D. Müller, P. Nimis, C. O'Malley, E. Powell, K. Priestley, R. Remm, T. Schlegel, D. Schutt, O. Shorttle, R. Skirrow, E. Smith, S. Stephenson, Y. Takei, C.-Y. Tien, N. White and J. Winterbourne for their assistance and discussions. S. Lebedev provided helpful feedback on an early draft of this work. M.J.H. acknowledges support from the National Aeronautics and Space Administration (grant NNX17AE17G) and the Donors of the American Chemical Society Petroleum Research Fund (59062-DNI8). F.D.R. acknowledges support from the Schmidt Science Fellows program, in partnership with the Rhodes Trust. K.C. and D.L.H. publish with permission of the CEO of Geoscience Australia. Geoscience Australia eCat ID 132624. M.J.H. is indebted to J. Austermann and J. Mitrovica for personal guidance and affording him the freedom to pursue this research.

Author contributions

K.C. discovered this relationship. K.C. and M.J.H. conceived and designed the study. D.L.H., K.C., F.D.R. and M.J.H. compiled deposit databases. A.L.J. collated Australian xenolith data. A.L.J., F.D.R. and M.J.H. performed the thermobarometry and palaeogeotherm modelling. F.D.R. and M.J.H. developed the shear-wave to temperature conversion scheme. F.D.R. calibrated anelasticity parameterizations. M.J.H. generated lithospheric thickness maps, performed statistical tests, made figures and compiled supplementary information. S.G., M.J.H. and K.C. investigated implications of rifting continental lithosphere. The paper was written by K.C. and M.J.H., with guidance from all authors.

Competing interests

The authors declare no competing interests.

Additional information

Extended data is available for this paper at https://doi.org/10.1038/s41561-020-0593-2.

Supplementary information is available for this paper at https://doi.org/10.1038/s41561-020-0593-2.

Correspondence and requests for materials should be addressed to M.J.H. or K.C.

Peer review information Primary Handling Editor: Rebecca Neely.

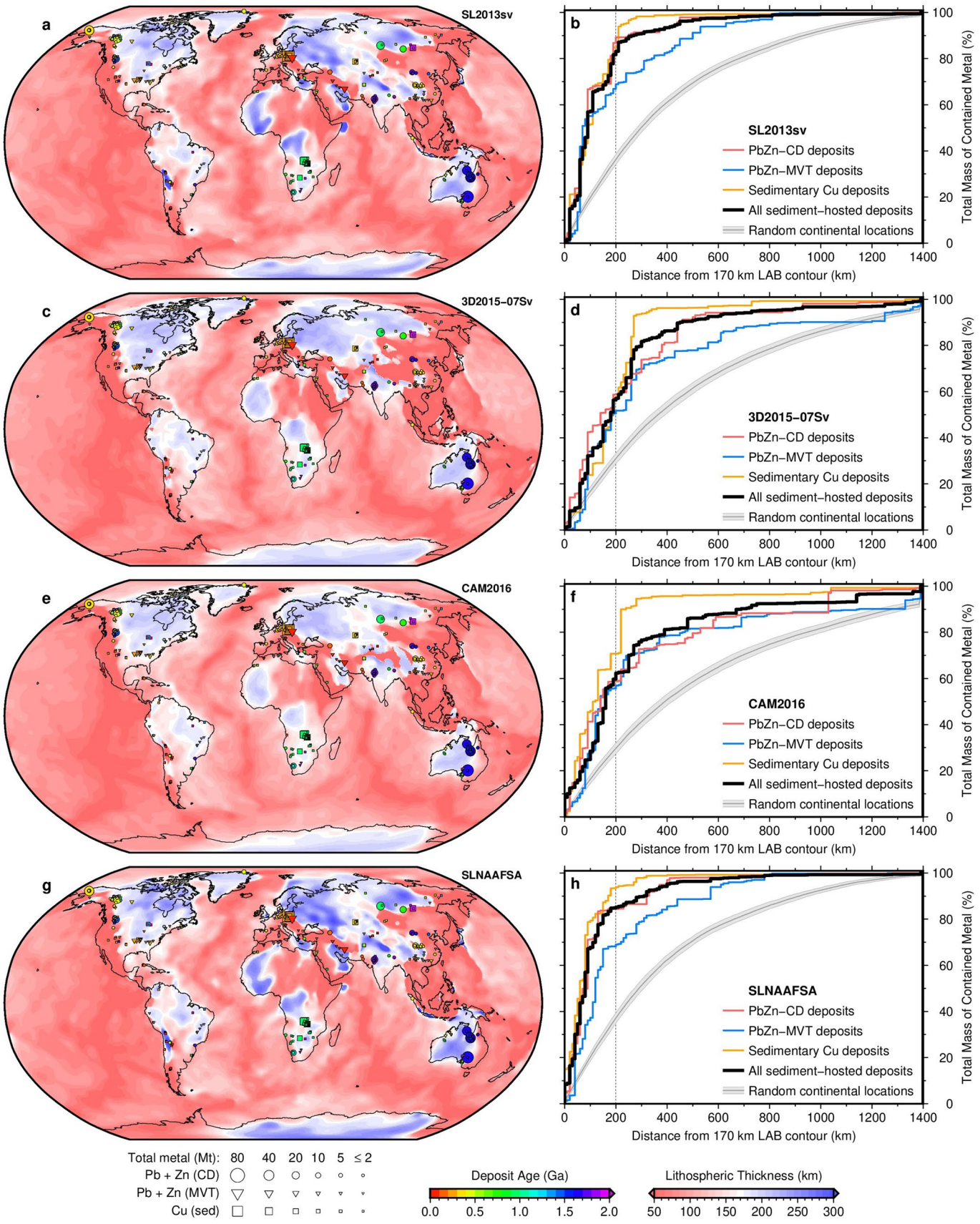

Extended Data Fig. 1 | See next page for caption.

Extended Data Fig. 1 | Global lithospheric thickness maps obtained from calibration of four upper mantle surface wave tomography models. (**a**) **SL2013sv** model.[30] Symbols = deposit locations; area proportional to estimate of total contained mass of metal (Mt = megatonnes); unknown deposit size given 2 Mt symbol; colour = ore body formation age (billion years); unknown age plotted in grey; circles = clastic-dominated lead-zinc (PbZn-CD); triangles = Mississippi Valley type lead-zinc (PbZn-MVT); squares = sedimentary copper (Cu-sed). (**b**) Associated CDFs for sediment-hosted deposits and random continental locations. (**c**-**d**) Same for the **3D2015-07Sv** model.[70] (**e**-**f**) Same for the **CAM2016** model.[71,72] (**g**-**h**) Same for the **SLNAAFSA** model, generated by blending regional updates from North America (**SL2013NA**[73]), Africa (**AF2019**[74]), and South America (**SA2019**[75]) into the global **SL2013sv** model.[30] Note that CDFs for all tomography models show a significant difference from the distribution of random continental locations.